JM PAPERS

Energy transfer and third-order law in forced anisotropic magneto-hydrodynamic turbulence with hyper-viscosity

Bin Jiang[1,2], **Cheng Li**[1,2], **Yan Yang**[3,†], **Kangcheng Zhou**[1,2,4], **William H. Matthaeus**[3] **and Minping Wan**[1,2,†]

[1]Guangdong Provincial Key Laboratory of Turbulence Research and Applications, Department of Mechanics and Aerospace Engineering, Southern University of Science and Technology, Shenzhen 518055, PR China

[2]Guangdong-Hong Kong-Macao Joint Laboratory for Data-Driven Fluid Mechanics and Engineering Applications, Southern University of Science and Technology, Shenzhen 518055, PR China

[3]Department of Physics and Astronomy, University of Delaware, DE 19716, USA

[4]Department of Mechanical Engineering, The University of Hong Kong, 999077, PR China

The third-order law links energy transfer rates in the inertial range of magneto-hydrodynamic (MHD) turbulence with third-order structure functions. Anisotropy, a typical property in the solar wind, challenges the applicability of the third-order law with the isotropic assumption. To shed light on the energy transfer process in the presence of anisotropy, we conducted direct numerical simulations of forced MHD turbulence with normal and hyper-viscosity under various strengths of the external magnetic field (B_0), and calculated three forms of third-order structure function with or without averaging of the azimuthal or polar angles with respect to B_0 direction. Correspondingly, three estimated energy transfer rates were obtained. The result shows that the peak of normalized third-order structure function occurs at larger scales closer to the B_0 direction, and the maximum of longitudinal transfer rates shifts away from the B_0 direction at larger B_0. Compared with normal viscous cases, hyper-viscous cases can attain better separated inertial range, thus facilitating the estimation of the energy cascade rates. We find that the widespread use of the isotropic form of the third-order law in estimating the energy transfer rates is questionable in some cases, especially when the anisotropy arising from the mean magnetic field is inevitable. In contrast, the direction-averaged third-order structure function properly accounts for the effect of anisotropy and predicts the energy transfer rates and inertial range accurately, even at very high B_0. With limited statistics, the third-order structure function shows a stronger dependence on averaging of azimuthal angles than the

† Email addresses for correspondence: yanyang@udel.edu, wanmp@sustech.edu.cn

time, especially for high B_0 cases. These findings provide insights into the anisotropic effect on the estimation of energy transfer rates.

Key words: MHD turbulence, turbulence theory

1. Introduction

Magneto-hydrodynamic (MHD) turbulence commonly exists in nature, such as the solar wind with high Reynolds numbers (Coleman & Paul 1968; Jokipii & Hollweg 1970; Parker 1979; Matthaeus & Goldstein 1982; Tu & Marsch 1995; Bruno & Carbone 2013), on which we focus here. From the engineering perspective, the solar wind has an influence on the weather in space, where it impacts the functioning of satellites. For fundamental research, the cross-scale energy transfer is an important process for the analysis and modelling of MHD turbulence. In the classical energy cascade scenario, energy is transferred from large to small scales at a constant rate, which is finally dissipated at the dissipation range (De Kármán & Howarth 1938; Taylor 1938; Kolmogorov 1941*b*,*a*; Kraichnan 1971). This picture has been adapted to MHD turbulence (Hossain *et al.* 1995; Politano & Pouquet 1998). It is trivial to obtain the dissipation rate in terms of *ad hoc* viscosity and resistivity, as implemented for example, in MHD simulations. However, space plasmas often behave as collisionless plasmas, for which the classical viscosity and resistivity become inapplicable, and therefore also inapplicable are the viscous and resistive dissipation rates. In the absence of a simple closed expression for the dissipation function, there has been increasing interest in resorting to the cross-scale energy transfer process to quantify the energy transfer rate in the inertial range (sometimes loosely called the cascade rate). For example, starting from the von Kármán–Howarth (vKH) equation (De Kármán & Howarth 1938; Monin & Yaglom 1975; Frisch 1995), a four-fifths (4/5) law, originally derived by Kolmogorov in hydrodynamic turbulence assuming statistical isotropy, links the dissipation rate with the third-order moment of longitudinal velocity increments (Kolmogorov 1941*b*), i.e. $\langle (\delta u_l)^3 \rangle$. This law was modified in a slightly more general form, a four-thirds law (Monin & Yaglom 1975; Frisch 1995; Antonia *et al.* 1997), by replacing the second-order moment of the longitudinal velocity increments with the sum of the square of the three velocity increments, i.e. $\langle \delta u_l | \delta \boldsymbol{u} |^2 \rangle$. An analogy of this law, also called the third-order law here, in incompressible MHD turbulence was derived by Politano & Pouquet (1998) under the assumption of statistical isotropy.

Given that turbulence is frequently simplified, e.g. assumed to be isotropic and incompressible, in most treatises on the energy transfer process, it is natural to enquire about the effects introduced by implementing other realistic complexities. For example, the isotropic third-order law has been generalized to take into account corrections from anisotropy (Podesta 2008; Osman *et al.* 2011; Stawarz *et al.* 2011; Verdini *et al.* 2015), compressibility (Carbone *et al.* 2009; Kritsuk *et al.* 2009; Banerjee *et al.* 2016; Hadid, Sahraoui & Galtier 2017; Yang *et al.* 2017; Andrés *et al.* 2019), solar wind shear (Wan *et al.* 2009, 2010) and expansion (Gogoberidze, Perri & Carbone 2013; Hellinger *et al.* 2013) and the Hall effect (Hellinger *et al.* 2018; Ferrand *et al.* 2019, 2022; Bandyopadhyay *et al.* 2020). Moreover, in solar wind turbulence, the cross-helicity plays an important role in energy transfer. Briard & Gomez (2018) studied the cross-helicity effect on total energy in the incompressible, decay and isotropic MHD turbulence, and reported that the cross-helicity spectrum scales as $k^{-5/3}$ at large Reynolds number but close to k^{-2} in low Reynolds number, where k is the wavenumber.

Anisotropy is inherent in turbulence threaded by a guiding magnetic field B_0 e.g. (Shebalin, Matthaeus & Montgomery 1983; Matthaeus *et al.* 1996; Horbury, Forman & Oughton 2008; Oughton *et al.* 2015), as in the solar wind. Oughton & Matthaeus (2020) reviewed the critical-balance theory in anisotropic MHD turbulence, including the energy spectrum scaling with $k_\parallel \sim k_\perp^{2/3}$. Here, we seek to systematically investigate the effect of anisotropy on the cross-scale energy transfer in the inertial range. It is widely accepted that the cross-scale energy transfer is suppressed along the parallel direction with respect to the mean magnetic field, which has been shown explicitly in terms of third-order structure functions using MHD turbulence simulations (Verdini *et al.* 2015). By computing the divergence of third-order structure functions along different directions of the separation vectors or lags, Verdini *et al.* (2015) characterizes the anisotropy of energy transfer and the so-obtained transfer rate depends on the angle between B_0 and the direction of lags. Therefore, the isotropic third-order law, although widely used in solar wind studies, is seriously flawed in that it does not take into account the angular dependence of energy transfer in anisotropic MHD turbulence. The presence of this anisotropy impacts in particular experimental estimations of energy transfer, as exemplified by the upcoming Helioswarm solar wind mission (Matthaeus *et al.* 2019; Spence 2019).

To expand the applicability of the third-order law for anisotropic MHD turbulence, the most straightforward way to proceed would be to directly compute the divergence of the energy-flux vector. The energy-flux vector is actually the third-order structure function, and its projection along the lag direction is used in the isotropic third-order law, wherein the energy-flux vector in the inertial range is nearly radial in lag space. On the one hand, an accurate determination of this divergence form requires information at all points in three-dimensional (3-D) lag space, necessitating simultaneous multi-point measurements that span 3-D spatial directions. For instance, Yoshimatsu (2012) explored direction-average impact on the 4/5 law with the forcing in the velocity field. Even without the external mean magnetic field, the local anisotropy still exists as per Milano *et al.* (2001). By comparing the averaging of the third-order structure function on a spherical surface with one direction, Yoshimatsu (2012) found that directional anisotropy can substantially affect the performance of the 4/5 law. With imposing external mean magnetic fields, Ferrand *et al.* (2022) made a comparison between decompositions in the axisymmetric and isotropic projections. They found that, without considering the parallel components of the vectorial third-order structure function to the B_0 direction, the estimation of the dissipation rate is less accurate than the isotropic projection. On the other hand, the requirement of a 3-D lag space to calculate the divergence is obviously not feasible with single-spacecraft data and even with multi-spacecraft data due to the small number of available lag directions. To overcome the difficulty, Podesta, Forman & Smith (2007) and Galtier (2009) modified the isotropic third-order law with an external B_0, employing additional assumptions. But we do not implement these theories due to their general complexity. The divergence form of the energy-flux vector can be simplified under certain symmetries. For example, in rotating turbulence having azimuthal symmetry with respect to the rotational axis (Yokoyama & Takaoka 2021) and the anisotropic MHD turbulence having azimuthal symmetry with respect to the guiding magnetic field (Alexakis *et al.* 2007), the divergence form can be simplified by integration over the azimuthal angle. Another simplification was realized originally in hydrodynamic turbulence by solid angle averaging over all possible orientations of the lag vector (Nie & Tanveer 1999; Taylor, Kurien & Eyink 2003), which was then adapted for MHD turbulence (Wan *et al.* 2009; Osman *et al.* 2011). Recently, Wang *et al.* (2022) investigated such a directional average of the third-order law over a number of lag directions on a spherical

surface. In comparison with the isotropic third-order law, this direction-averaged version attains a more accurate energy dissipation rate and will be called the direction-averaged third-order law hereafter.

These preliminary demonstrations provide supporting but incomplete evidence to develop a discrete formulation that is representative of the anisotropic energy transfer process and is applicable to both numerical analyses and observational realizations such as Helioswarm (Spence 2019). To advance these issues, here, we conduct a systematic study of the angular dependence of the third-order law and the effect of the number of samples over directions spanning the solid angle with various strengths of the external mean magnetic field (B_0). Besides the direction averaging, the effect of time averaging is also investigated. Concerning the energy cascade process in the inertial range, one requires the existence of a range of scales, in which the dynamics is dominated by inertia terms and is well separated from both the energy-containing range and the dissipation range. Hyper-viscosity is often used to extend the inertial range, which attains a similar Reynolds number with lower computational costs. Spyksma, Magcalas & Campbell (2012) compared the characteristics of the normal with hyper-viscous simulations, and formulated the characteristic length scale and Reynolds number for the hyper-viscous case. Biskamp & Müller (2000) conducted isotropic MHD simulation with hyper-viscosity to obtain an elongated inertial range well separated from the dissipation range. They reported that the bottleneck effect is invisible in the structure function profiles, but can be identified in the energy spectra, introducing a hump at the end of the inertial range. Beresnyak & Lazarian (2009) simulated anisotropic MHD turbulence with hyper-viscosity and various B_0, and claimed that the bottleneck effect is inhibited by external magnetic fields in energy spectra. Here, we also conduct numerical simulations of anisotropic MHD turbulence with hyper-viscosity, but the emphasis is on the impact of hyper-viscosity on the evaluation of the third-order law with varying external magnetic fields.

The structure of the paper is as follows: in § 2, the numerical method will be introduced, including the governing equations, simulation configurations and several characteristics. A brief review of the third-order law is given in § 3. In § 4, the effects of hyper-viscosity on structure functions are discussed, and the effects of directional and time averaging on the third-order law will be given. The key findings will be listed in the conclusion.

2. Numerical methods

2.1. *Governing equations*

The hyper-viscosity modified governing equation for the simulation of incompressible MHD turbulence is written as (Biskamp 2003)

$$\frac{\partial \boldsymbol{v}}{\partial t} + (\boldsymbol{v} \cdot \nabla)\boldsymbol{v} = -\nabla\left(p + \frac{|\boldsymbol{b}|^2}{2}\right) + (\boldsymbol{b} \cdot \nabla)\boldsymbol{b} + (\boldsymbol{B_0} \cdot \nabla)\boldsymbol{b} + (-1)^{h+1}\nu_h\nabla^{2h}\boldsymbol{v} + \boldsymbol{f_v},$$
(2.1)

$$\frac{\partial \boldsymbol{b}}{\partial t} + (\boldsymbol{v} \cdot \nabla)\boldsymbol{b} = (\boldsymbol{b} \cdot \nabla)\boldsymbol{v} + (\boldsymbol{B_0} \cdot \nabla)\boldsymbol{v} + (-1)^{h+1}\eta_h\nabla^{2h}\boldsymbol{b},$$
(2.2)

$$\nabla \cdot \boldsymbol{v} = 0,$$
(2.3)

$$\nabla \cdot \boldsymbol{b} = 0,$$
(2.4)

where $\boldsymbol{v}$ and $\boldsymbol{b}$ represent the velocity vector and the fluctuating magnetic field, respectively, $\boldsymbol{b}$ is scaled by $\sqrt{4\pi\rho}$ in Alfvén speed units, where ρ denotes the uniform mass density. An

974 A20-4

B_0	h	Grids	ε_v	ε_b	b_{rms}	$R_{\lambda,v}$	$R_{\lambda,b}$	$k_{max}\eta_{k,v}$	$\theta_v(°)$	Averaging period (T_e)
0	1	1024^3	0.59	1.39	0.88	290	89	1.86	62	[5 : 19]
2	1	1024^3	0.78	1.07	1.11	295	164	1.73	73	[5 : 17]
5	1	1024^3	0.81	0.80	1.02	467	166	1.71	83	[9 : 18]
0	2	512^3	0.67	1.24	0.92	846	255	1.73	55	[15 : 30]
2	2	512^3	0.77	1.12	1.14	951	473	1.71	72	[8 : 68]
5	2	512^3	0.83	1.02	1.08	2415	435	1.70	83	[200 : 275]

Table 1. Configuration set-up of normal viscous and hyper-viscous simulations at different external mean magnetic fields (B_0). Here, h denotes the order of the hyper-viscosity; ε_v and ε_b represent the kinetic and magnetic dissipation rates, respectively; $R_{\lambda,v}$ and $R_{\lambda,b}$ are the kinetic and magnetic Taylor Reynolds numbers, respectively; $k_{max}\eta_{k,v}$ illustrates the grid resolution, where $\eta_{k,v}$ and k_{max} are respectively the Kolmogorov length scale and the maximum resolved wavenumber (a third of the total grid in one direction); θ_v describes the anisotropic intensity as in Shebalin *et al.* (1983); T_e refers to the large-eddy turnover time at $B_0 = 0$; b_{rms} indicates the magnetic field fluctuation in the stationary period.

external mean magnetic field, $\boldsymbol{B}_0 = B_0\boldsymbol{e_z}$, is imposed along the z-direction. Its magnitude is defined with respect to the initial magnetic fluctuation, whose root mean square (r.m.s.) is $b_{rms} \approx 1$. Here, p is the thermal pressure; ν_h and η_h denote the kinetic viscosity and the magnetic resistivity coefficients, respectively. The power h is the order of hyper-viscosity, where $h = 1$ represents normal viscosity and $h > 1$ represents hyper-viscosity. An external force, $\boldsymbol{f_v}$, is added to the kinetic governing equation to achieve a statistically stationary state. The forcing is solenoidal to avoid introducing compression into the velocity field.

2.2. *Configuration set-up*

We solve the Fourier-space version of the governing equations via the pseudo-spectral method with de-aliasing by the two-thirds rule. The computational domain is a cube of dimension $[0, 2\pi]^3$ with periodic boundary conditions in all directions. The second-order Adam–Bashforth scheme is employed for time advancement. The external force, $\boldsymbol{f_v}$, acts only on the first two wavenumber shells, i.e. $k = 1$ and $k = 2$, without affecting the inertial range, where k is the norm of the wavenumber vector, $\boldsymbol{k}$. The forcing is achieved by keeping a constant energy injection rate. Mathematically, it is a random, Gaussian-distributed and $\delta(t)$-correlated function as in Yang *et al.* (2021). The system is driven at wavenumbers 1 and 2, and scales longer than this are not included. Therefore, there is no large-scale 'infrared' region in the simulation. All runs are initialized with random velocity and magnetic fluctuations within the wavenumber band $k \in [1, 5]$, with spectra proportional to $1/[1 + (k/k_0)]^{11/3}$ and $k_0 = 3$ representing the knee of the spectrum. The initial kinetic and magnetic energies are equal, i.e. $E_v = E_b = 0.5$. The cross-helicity is almost zero. Equal viscosity and resistivity (i.e. the magnetic Prandtl number is unity) are used for all simulations.

To study the anisotropic energy transfer process in the inertial range, we initialize our simulations with a range of external mean magnetic fields, B_0, and two types of viscosity. These runs are grouped into two series and more details are listed in table 1. The first series of runs is conducted on 1024^3 grids using normal viscosity (i.e. $h = 1$), $\nu_h = 8 \times 10^{-4}$, and the second series of runs is conducted on 512^3 grids using hyper-viscosity at order $h = 2$, $\nu_h = 2 \times 10^{-7}$. A higher order, $h = 3$, was tested, while the bottleneck effect becomes more obvious as per Frisch *et al.* (2008), indicated by a higher peak in the compensated energy spectra. The present hyper-viscosity with a lower order achieves a

separated inertial range from the dissipation range without introducing strong bottleneck effects. All simulations are fully resolved with $k_{max}\eta_{k,v} > 1.5$, where k_{max} is the largest resolved wavenumber, and the kinetic Kolmogorov length scale, $\eta_{k,v} = (\nu_h^3/\varepsilon_v)^{1/(6h-2)}$, where ε_v is the kinetic dissipation rate. The time to reach a statistically stationary state and the sampling period are listed in table 1, and all cases are sampled with 0.5 large-eddy turnover time (T_e). Throughout the paper, the time will be in units of T_e at $B_0 = 0$. The cases without or with a relatively weak external mean magnetic field, i.e. $B_0 = 0$ and 2, reach the statistically steady state earlier than the higher B_0 cases. To obtain the following statistical properties, we use 20 time frames over $10T_e$ for the normal viscous cases, and for the hyper-viscous cases, 30, 120 and 150 time frames over $15T_e$, $60T_e$ and $75T_e$ at $B_0 = 0$, 2 and 5, respectively.

More observables for all simulations are listed in table 1 and they are time averaged. The kinetic dissipation rate, ε_v, and the magnetic dissipation rate, ε_b, are calculated as

$$\varepsilon_v = \nu_h \sum_k k^{2h}\langle|\hat{\boldsymbol{u}}(\boldsymbol{k}, t)|^2\rangle, \quad \varepsilon_b = \eta_h \sum_k k^{2h}\langle|\hat{\boldsymbol{b}}(\boldsymbol{k}, t)|^2\rangle, \tag{2.5a,b}$$

where $\hat{\boldsymbol{u}}$ and $\hat{\boldsymbol{b}}$ denote the velocity and magnetic vectors in the Fourier space. The operator $\langle\cdot\rangle$ denotes the ensemble average, which is identical to the space average for homogeneous turbulence. The kinetic dissipation rate increases with B_0, while the magnetic dissipation rate decreases. Note that the values of the cascade rate, ε_v and ε_b, are strongly influenced by the energy injection by the forcing term.

To quantify the anisotropy at different B_0, the variable θ_v, originally introduced by Shebalin *et al.* (1983), is used, $\tan^2\theta_v = \sum k_\perp^2|\boldsymbol{u}(\boldsymbol{k}, t)|^2/\sum k_z^2|\boldsymbol{u}(\boldsymbol{k}, t)|^2$. In the isotropic case, θ_v equals $54°$. For an extreme case with all energy in the plane perpendicular to the B_0 direction, θ_v is close to $90°$. Table 1 shows that θ_v is larger at a higher B_0 value. We also calculated the anisotropy angles for the magnetic field and in all cases the values were very similar to those of the velocity field. In addition, we calculated anisotropy of the Reynolds tensors $\langle b_i b_j\rangle$ and $\langle u_i u_j\rangle$ decomposed by wavenumber (Zhai & Yeung 2018), and found that both exhibit anisotropies that persist to the small scales.

The individual spectra for the kinetic and magnetic energies at $B_0 = 0$ are shown in figure 1. We found that the kinetic energy is indeed scaled with the $-3/2$ slope, and the magnetic energy shows $k^{-5/3}$ scaling as per (Alexakis 2013). Figure 1 also shows the reduced spectra of total energy $E = E_v + E_b$ in the $k_\parallel$ and $k_\perp$ planes for the normal and hyper-viscous simulations, where $k^{-5/3}$ power law is also shown for reference. The parallel and perpendicular spectra are defined as $E(k_\parallel) = \sum_{k_\perp} E(k_\parallel, k_\perp); E(k_\perp) = \sum_{k_\parallel} E(k_\parallel, k_\perp)$; respectively. It is clear that the parallel spectrum is suppressed and the perpendicular spectral transfer is stronger than the parallel transfer with increasing B_0. This reflects the decrease of the dissipation rate with the increasing of B_0, as listed in table 1. One may observe that higher energy resides in the first $\sim$3 wave modes at larger B_0 as reported in Alexakis *et al.* (2007). The inertial range is roughly viewed as the range of scales over which the spectrum fits well with the $k^{-5/3}$ power law. As expected, the simulations with hyper-viscosity realize an elongated inertial range.

3. Direction-averaged third-order law

This section describes three types of averaging relevant to the third-order law. Starting from the vKH equation (De Kármán & Howarth 1938; Monin & Yaglom 1975; Frisch 1995), a general form of the third-order law will be derived. Considering that the present
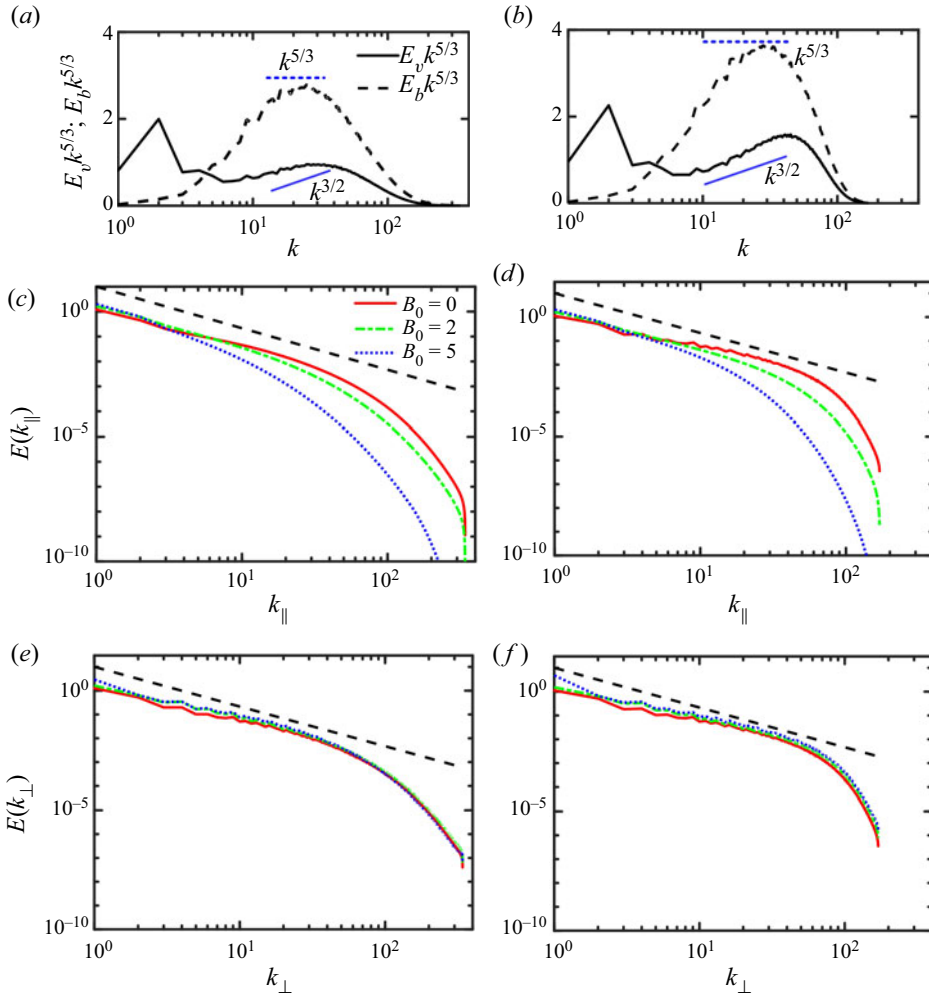
Figure 1. Spectra of (a,c,e) normal viscous simulations and (b,d,f) hyper-viscous simulations: (a,b) kinetic and magnetic spectra at $B_0 = 0$; (c,d) parallel and (e,f) perpendicular reduced spectra of total energy, $E(k_\parallel)$ and $E(k_\perp)$ at $B_0 = 0, 2, 5$.

study relates to the effects of an externally supported mean magnetic field, the three types of averaging applied to the general form will be discussed under different assumptions regarding anisotropy.

The vKH equation is typically composed of the time rate of change of energy, energy transfer across scales and energy dissipation terms, which respectively dominate at energy injection, inertial and dissipation scales. These contributions are evident in the vKH equation itself

$$\frac{\partial}{\partial t}\langle(\delta z^\pm)^2\rangle = -\boldsymbol{\nabla}_l \cdot \langle \delta z^\mp |\delta z^\pm|^2\rangle + 2\nu\nabla_l^2\langle(\delta z^\pm)^2\rangle - 4\varepsilon^\pm. \tag{3.1}$$

Here, $\boldsymbol{\nabla}_l$ denotes derivatives in the lag vector (l) space; $\boldsymbol{Y}^\pm = \langle \delta z^\mp |\delta z^\pm|^2\rangle$ is the third-order structure function, also called the (Yaglom) energy-flux vector with the

974 A20-7

Elsässer variable ($z^\pm = u \pm b$) increment being defined as $\delta z^\pm(x, l) = z^\pm(x + l) - z^\pm(x)$ and $\varepsilon^\pm = \nu_h \sum_k k^{2h} \langle |\hat{z}^\pm(k, t)|^2 \rangle$ represent the mean dissipation rates of Elsässer energies.

In the inertial range with negligible contribution from non-stationary and dissipative terms in (3.1), the cross-scale energy transfer is expressed as

$$\nabla_l \cdot Y^\pm = \nabla_l \cdot \langle \delta z^\mp |\delta z^\pm|^2 \rangle = -4\varepsilon^\pm. \tag{3.2}$$

Note that, after ensemble averaging in the homogeneous turbulence, no dependence of $Y^\pm$ on the position x remains, and $\varepsilon^\pm$ is independent of both position x and lag l.

In anisotropic conditions, as in the present study with imposed external mean magnetic field, (3.2) can be reformulated by taking a volume integral in a sphere of radius l as follows:

$$\iiint_{|l| \leq l} \nabla_l \cdot Y^\pm \, dV = \iiint_{|l| \leq l} -4\varepsilon^\pm \, dV. \tag{3.3}$$

Using Gauss's theorem, (3.3) can be written as a surface integral

$$\oint_{|l|=l} Y_l^\pm \, dS = \iiint_{|l| \leq l} -4\varepsilon^\pm \, dV = -\frac{16\pi}{3} \varepsilon^\pm l^3, \tag{3.4}$$

where $Y_l^\pm = \langle \delta z_l^\mp |\delta z^\pm|^2 \rangle$ is the projection of the energy-flux vector along l; $\delta z_l^\mp = \delta z^\mp \cdot l/l$, and l is the norm of l. In spherical coordinates, (3.4) can be written as

$$\frac{1}{4\pi} \int_0^{2\pi} \int_0^\pi Y_l^\pm \sin\theta \, d\theta \, d\phi = -\frac{4}{3} \varepsilon^\pm l, \tag{3.5}$$

where θ represents the polar angle and ϕ the azimuthal angle. Given that no assumptions about rotational symmetry are made in going from (3.2) to (3.5), the physical content of (3.5) is as general as the derivative form (3.2). The full generality of (3.5) follows from the rigorous theorem given by Nie & Tanveer (1999) and restated in more accessible terms by Taylor *et al.* (2003) and Wang *et al.* (2022). However, (3.5) is simpler in the sense that accurate determination of the integration only requires information on the spherical surface spanned by the (θ, ϕ) coordinates in the 3-D lag space.

The most general form of $Y_l^\pm$ should be a function of l, θ and ϕ, i.e. $Y_l^\pm(l, \theta, \phi)$. However, there is no universal expression of $Y_l^\pm(\theta, \phi)$ so far, as little information is available on its variation with turbulence parameters. Previous studies have either been limited to the purely isotropic assumption (i.e. $Y_l^\pm$ is independent of θ and ϕ) or treated anisotropic turbulence with azimuthal symmetry (i.e. $Y_l^\pm$ is independent of ϕ) as implemented, for example by Stawarz *et al.* (2009). Under the isotropic assumption, (3.5) can be reduced to

$$\frac{1}{4\pi} Y_{l,isotropic}^\pm \int_0^{2\pi} \int_0^\pi \sin\theta \, d\theta \, d\phi = Y_{l,isotropic}^\pm = -\frac{4}{3} \varepsilon^\pm l. \tag{3.6}$$

To better understand the anisotropic energy transfer in the inertial range, here, we provide a systematic study of the $Y_l^\pm$ dependence on θ and ϕ with different guide field magnitudes. Specifically, three forms of $Y_l^\pm$ are discussed:

(i) The general form of the third-order structure function for every lag vector $l = (l, \theta, \phi)$ in 3-D lag space

$$Y_l^\pm(\theta, \phi) = \langle \delta z_l^\mp |\delta z^\pm|^2 \rangle = Y_l^\pm(\theta_i, \phi_j), \tag{3.7}$$

represents a local radial or longitudinal energy transfer, and 'local' means at the specific azimuthal and polar angles, while the total radial energy transfer is the

sum of the contributions, i.e. (3.7), from all azimuthal ϕ and polar θ directions at the same lag. Due to the axisymmetric external mean magnetic field, the range of θ is $[0°, 90°]$. Lag vectors in 37 directions, uniformly spaced in azimuthal and polar angles ($\Delta\theta = 15°$ and $\Delta\phi = 60°$), are used to cover the sphere. Note that, at $\theta = 0°$, all these 6 azimuthal angles collapse into one direction. A 3-D Lagrangian interpolation was used to obtain the data not located at grid points. Separate estimates are made for each of 37 directions, i.e. $Y_l^{\pm}(\theta_i, \phi_j)$, $\theta_i \in [0° : 15° : 90°]$ and $\phi_j \in [0° : 60° : 300°]$.

(ii) The azimuthal-averaged form of the third-order structure function

$$\widetilde{Y_l^{\pm}}(\theta_i) = \frac{1}{2\pi} \int_0^{2\pi} Y_l^{\pm}(\theta_i, \phi) d\phi \approx \frac{\sum_{j=1}^{N_j} Y_l^{\pm}(\theta_i, \phi_j)}{N_j}, \tag{3.8}$$

describes the anisotropy of the local radial energy transfer, and 'local' means at a specific polar angle, while the total transfer rate is the sum of the contributions, i.e. (3.8), from all polar θ directions at the same lag. Here, $N_j(= 6)$ represents the number of azimuthal angles. Following (3.7), separate estimates are made for each of 37 directions, and then averaged over 6 azimuthal directions.

(iii) The direction-averaged form of the third-order structure function

$$\overline{Y_l^{\pm}} = \frac{1}{4\pi} \int_0^{2\pi} \int_0^{\pi} Y_l^{\pm} \sin\theta \, d\theta \, d\phi \approx \frac{\sum_{j=1}^{N_j} \sum_{i=1}^{N_i} Y_l^{\pm}(\theta_i, \phi_j) \sin\theta_i}{N_j \sum_{i=1}^{N_i} \sin\theta_i}, \tag{3.9}$$

is rather general since it takes into account all possible anisotropy in both azimuthal and polar directions. Here, $N_i(=7)$ and $N_j(=6)$ represent the number of angles θ and ϕ. This direction-averaged form of the third-order structure function is derived directly from the vKH equation without the assumption of statistical isotropy and only depends on the lag length l. After normalizing $\overline{Y_l^{\pm}}$ with the lag $-4/3l$, it can represent an accurate estimation of the cross-scale energy transfer rate (or energy dissipation rate ε) and the inertial range.

The aforementioned description of the energy transfer in the three forms of third-order structure functions can provide estimations of the actual energy transfer rate to different degrees. For instance, (3.7) has been widely used in the observational measurements with one spacecraft. To clearly show the estimation of the energy transfer rate and the inertial range, the aforementioned three forms of the third-order structure functions, i.e. $Y_l^{\pm}$, $\widetilde{Y_l^{\pm}}$ and $\overline{Y_l^{\pm}}$, will be averaged on their $+$ and $-$ components and normalized with the lag and the actual cascade rate, i.e. $-\frac{4}{3}\varepsilon l$, where ε is the total cascade rate, $\varepsilon = (\varepsilon^+ + \varepsilon^-)/2 = \varepsilon_b + \varepsilon_v$. Here, the average on the $+$ and $-$ components considers the almost zero cross-helicity, as such these two components are statistically equal.

4. Results and discussion

This section will make a comparison between normal viscous and hyper-viscous cases and focus on the angular dependence of third-order structure functions under various strengths of the external magnetic field. In addition, the possible effect of time averaging will be discussed.
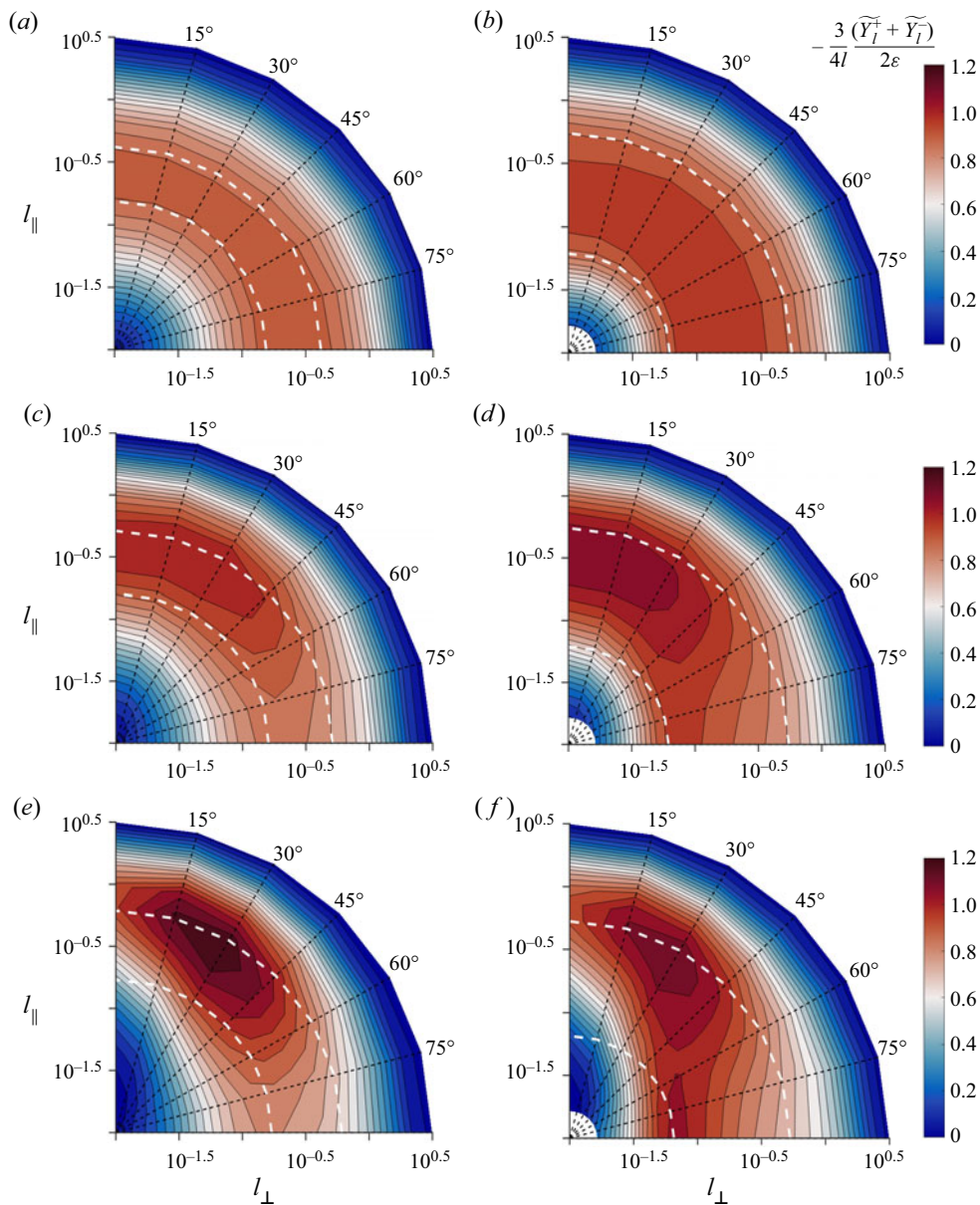
Figure 2. Comparison of normalized third-order structure functions, i.e. method II in (3.8) with $-3(\widetilde{Y_l^+} + \widetilde{Y_l^-})/(8\varepsilon l)$ between (a,c,e) simulations with normal viscosity and (b,d,f) simulations with hyper-viscosity with polar angles in the range $\theta = [0° : 15° : 90°]$. Here, $\theta = 0°$ represents the parallel direction relative to $\boldsymbol{B}_0$, and $\theta = 90°$ represents the perpendicular direction relative to $\boldsymbol{B}_0$. The white dashed lines represent the inertial range, identified with the direction-averaged form of third-order law, i.e. method III in (3.9), where $-3(\overline{Y_l^+} + \overline{Y_l^-})/(8\varepsilon l)$ is beyond a threshold, say 0.9. All contours are integrated over ϕ and time; (a,b) $B_0 = 0$, (c,d) $B_0 = 2$, (e,f) $B_0 = 5$.

4.1. *Effects of hyper-viscosity and polar angle dependence*

In anisotropic MHD turbulence with a mean magnetic field, the energy transfer is often deemed to be isotropic in the plane perpendicular to the B_0 direction, that is, $Y_l^{\pm}$ is ϕ independent. So as a first analysis, we integrate $Y_l^{\pm}$ over ϕ and time average over long statistically stationary periods and obtain a normalized third-order structure function as $-3(\widetilde{Y_l^+} + \widetilde{Y_l^-})/(8\varepsilon l)$.

Figure 2 shows contour of the averaged and normalized third-order structure functions for both normal viscous and hyper-viscous cases with various values of B_0. The inertial range is identified with the direction-averaged form of the third-order law, where $-3(\overline{Y_l^+} + \overline{Y_l^-})/(8\varepsilon l)$ is beyond a threshold, say 0.9, and marked with the white dashed lines. A straightforward observation is that the isotropic cases at $B_0 = 0$ present a distribution of the normalized structure functions that is essentially independent of polar angle θ. Unlike this isotropic case ($B_0 = 0$), the dark contour lines for $B_0 = 2$ and 5 do not distribute symmetrically. More specifically, the contour lines at small l (dark blue regions close to origins) are elongated along the parallel direction $\theta = 0°$, which can be interpreted as the anisotropy introduced by the mean magnetic field. The contour lines at large l (dark blue outer regions) approach a more circular conformation. This is not in conflict with the frequently observed picture of anisotropy in decaying MHD turbulence, as the present system is driven isotropically at large scales. The inertial range exists in the transition region between small and large scales, as marked with the white dashed lines. For non-zero B_0 cases, the peak value of the normalized third-order structure function at larger θ occurs at smaller scales, which is consistent with the results in Verdini *et al.* (2015) and Wang *et al.* (2022). The maximum radial transfer rate shifts away from the B_0 direction at larger B_0, with the corresponding θ of the maxima for $B_0 = 2$ and 5 at $\theta = 0°$ and $\theta = 30°$, respectively, which is clearer in figure 3.

We can see the clear difference between normal and hyper-viscous cases in figure 3, where the normalized third-order structure functions at $\theta \in [0° : 15° : 90°]$ are shown. Also shown is the normalized and direction-averaged third-order structure function, i.e. $-3(\overline{Y_l^+} + \overline{Y_l^-})/(8\varepsilon l)$. Even though the normalized third-order structure functions exhibit evident dependence on θ, the direction-averaged third-order law attains an accurate cascade rate with less than 5 % error for all cases. The plateau of the direction-averaged form in figure 3 gives a rough idea of the inertial range, which indicates that $l \in [0.15, 0.43]$ and $l \in [0.08, 0.55]$ at $B_0 = 0$ can be roughly identified as the inertial range for the normal and hyper-viscous cases, respectively. This elongated inertial range is also consistent with the estimates of the inertial range in figure 1, where $k = 2\pi/l$. Therefore, as expected, hyper-viscosity enables a wider inertial range than normal viscosity and the longer inertial range is beneficial to examine the third-order law.

The hyper-viscous cases show a similar polar angle dependence to the normal viscous cases at low B_0 (i.e. weak anisotropy). At $B_0 = 0$, the individual θ profiles in figure 3 overlap with the direction-averaged profile, indicating the applicability of the 1-D isotropic third-order law. As B_0 increases, they deviate from the direction-averaged profile. In particular, when B_0 is large enough (e.g. figure 3(*e,f*) with $B_0 = 5$), the third-order structure functions for the hyper-viscous cases exhibit distinct peak values from the normal viscous cases. For the normal viscous case, the third-order law tends to underestimate the cascade rate for $\theta > 45°$, and overestimate the cascade rate for $\theta < 45°$. As such, the maximum value of the estimated cascade rate is located at $\theta = 30°$, also shown in figure 2. In contrast, for the hyper-viscous case, the third-order law at $\theta \sim 90°$ overestimates the
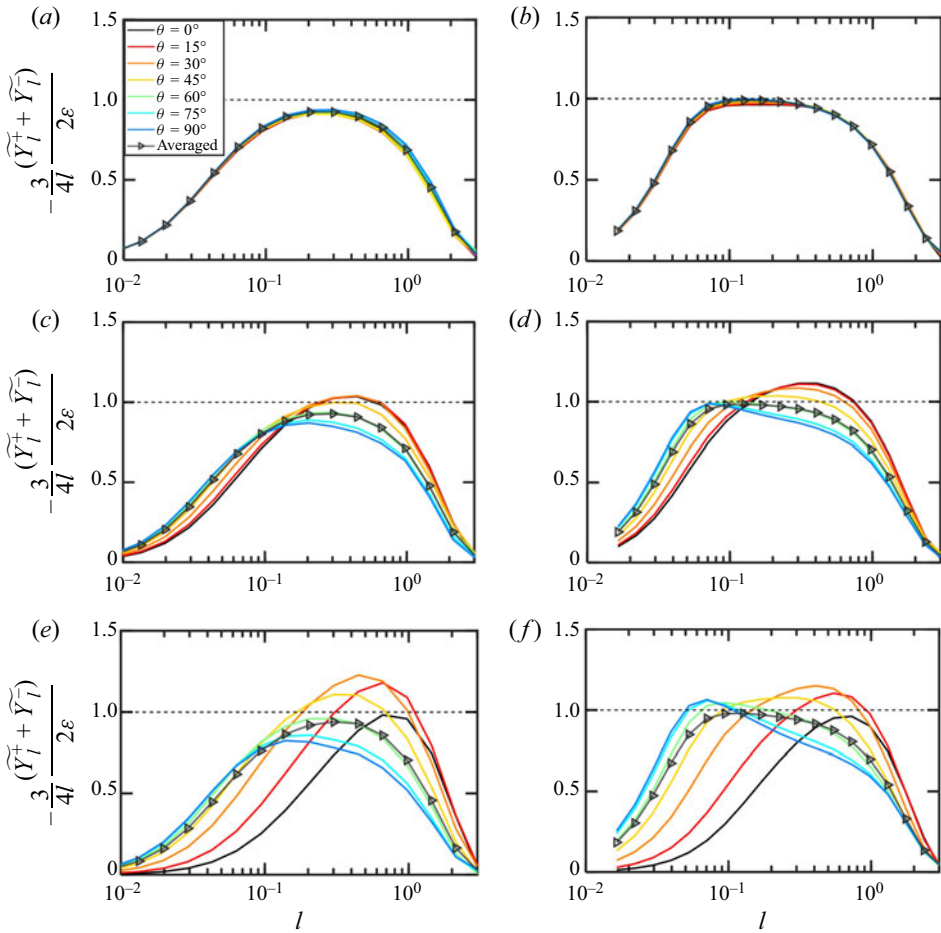
Figure 3. Comparison of normalized third-order structure functions, i.e. method II in (3.8) with $-3(\widetilde{Y_l^+} + \widetilde{Y_l^-})/(8\varepsilon l)$, at $B_0 = 0, 2, 5$ between (a,c,e) normal viscous and (b,d,f) hyper-viscous simulations with $\theta = [0° : 15° : 90°]$, and the solid line with triangles represents the direction-averaged profile, i.e. method III in (3.9) with $-3(\overline{Y_l^+} + \overline{Y_l^-})/(8\varepsilon l)$. All curves are averaged over ϕ and time. For non-zero B_0 the estimated transfer rate peaks at large scales for parallel angles, and at progressively smaller scales for perpendicular angles; (a,b) $B_0 = 0$, (c,d) $B_0 = 2$, (e,f) $B_0 = 5$.

cascade rate and the contour map in figure 2 exhibits two local maxima at $\theta = 30°$ and $\theta = 90°$. The maximum at $\theta = 90°$ could be attributed to the dissipation being concentrated at smaller scales due to hyper-viscosity. As we can see, the energy transfer changes gradually with angles and the most efficient transfer may not necessarily occur in the strictly perpendicular direction.

4.2. *Azimuthal angle dependence*

In this subsection, the hyper-viscous cases will be used to demonstrate the azimuthal dependence of the third-order structure function. Figure 4(a,c,e) shows the normalized third-order structure function at different θ and ϕ. It can be seen that the variability of third-order structure functions in the azimuthal and polar angles increases with the increase of B_0, indicated by the more scattered distribution of the profiles at higher B_0.
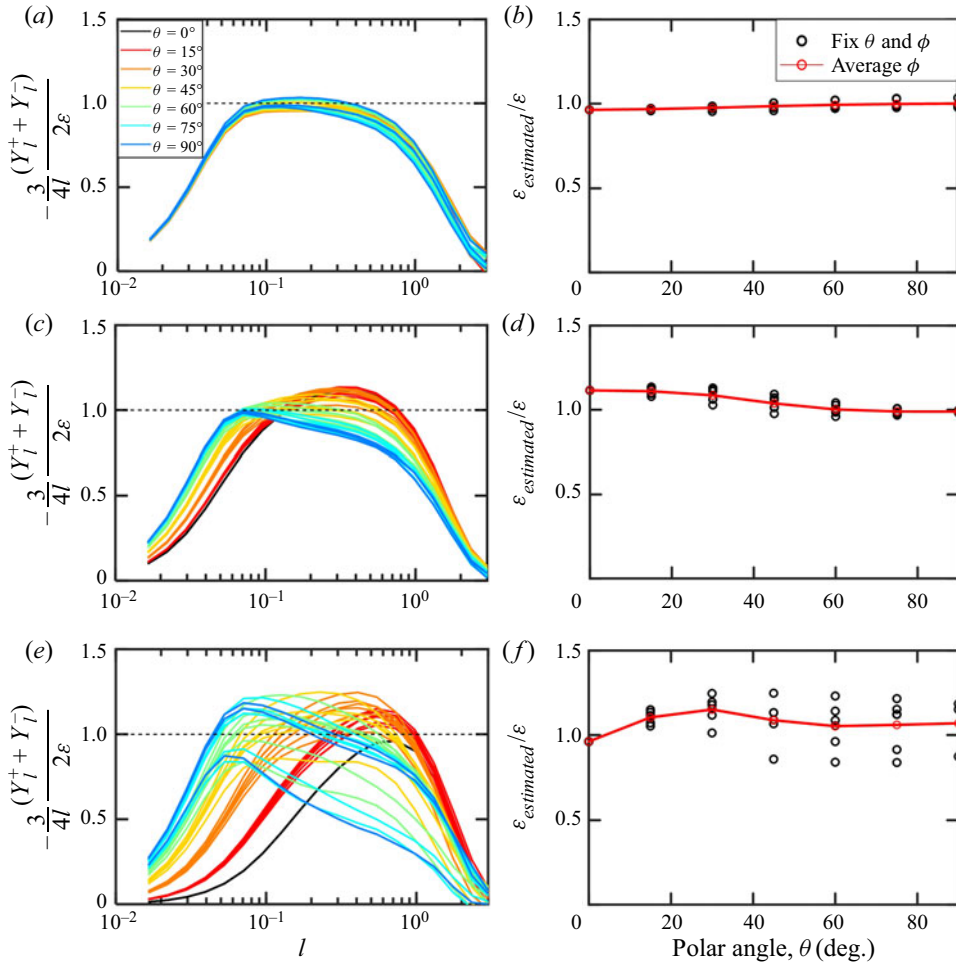
974 A20-12

Figure 4. (*a,c,e*) Normalized third-order structure functions, i.e. method I in (3.7) with $-3(Y_l^+ + Y_l^-)/(8\varepsilon l)$, for (*a,b*) $B_0 = 0$, (*c,d*) $B_0 = 2$ and (*e,f*) $B_0 = 5$ hyper-viscous cases at different θ and ϕ. Each series of colours represents a fixed θ and varied ϕ, e.g. green lines represent the results at $\theta = 60°$ and $\phi = [0° : 60° : 300°]$. (*b,d,f*) Estimated cascade rates from column (*a,c,e*) by extracting the peaks of each curve and then normalizing with the total dissipation rate, ε. The solid line with circles represents the averaged profile on the azimuthal direction. All curves are time averaged.

Specifically, at $B_0 = 0$, these individual lines almost collapse, indicating the isotropic features in both the polar and azimuthal directions. At $B_0 = 2$, the peak values of these lines are almost beyond unity. At $B_0 = 5$, the peaks vary beyond and below unity. To further quantify these departures from the actual cascade rates in table 1, figure 4(*b,d,f*) is plotted by using the peak of each profile, representing the estimated cascade rate. The distribution of these estimates, as marked with the dark circles, is more scattered at a larger B_0. At $B_0 = 2, 5$, the maximum estimated cascade rate can depart from the actual value by 10 % and 25 % and both at $\theta = 45°$. We expect this departure to be even greater at larger B_0. From the red line in figure 4(*b,d,f*), after doing the azimuthal average, the maximum departures from unity reduce to 3 % and 15 % at $B_0 = 2, 5$, respectively.

Theoretically, given that the number of frames is sufficient to compute a stable average, the averaged structure function should be independent of the azimuthal angles.
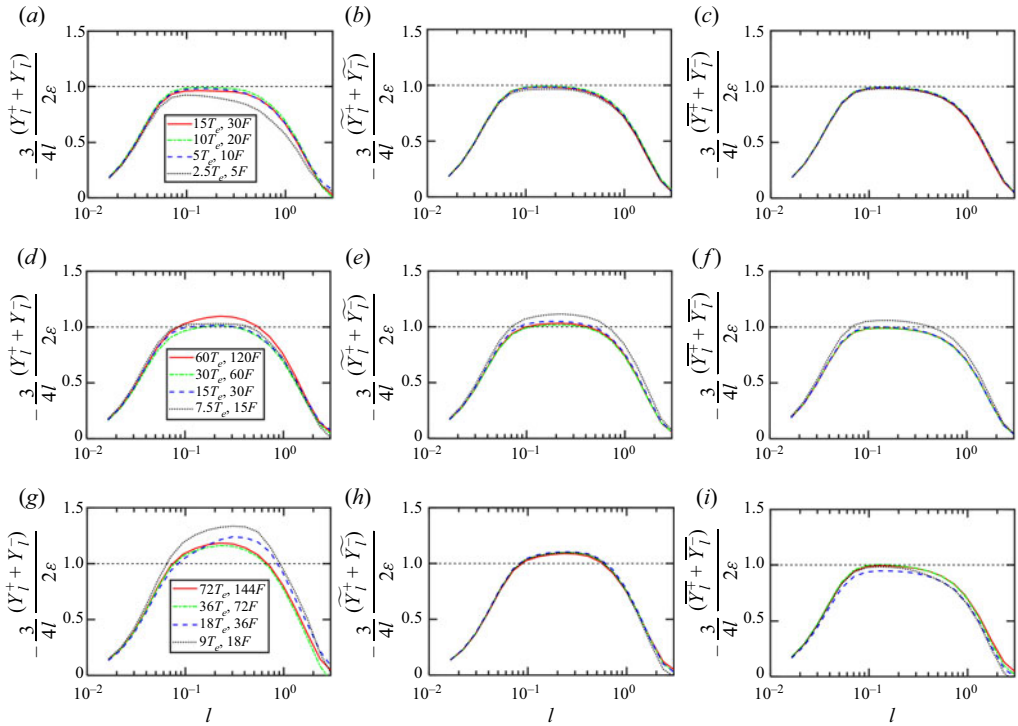
974 A20-13

Figure 5. Effects of the number of time frames on the calculation of the normalized third-order structure functions at $(a–c)$ $B_0 = 0$, $(d–f)$ $B_0 = 2$ and $(g–i)$ $B_0 = 5$ for the hyper-viscous cases. (a,d,g) Method I in (3.7) with fixed $\theta = \pi/4$; $\phi = \pi/3$. (b,e,h) Method II in (3.8) with fixed $\theta = \pi/4$ and azimuthal-averaged profiles. (c,f,i) Method III in (3.9) with direction-averaged profiles. Here, T_e denotes the large-eddy turnover time at $B_0 = 0$, and F represents the number of frames used in the time average. (a,d,g) Fixed $\theta = \pi/4$ and $\phi = \pi/3$. (b,e,h) Fixed $\theta = \pi/4$, Averaging ϕ. (c,f,i) Averaging θ and ϕ.

Therefore, when we describe energy transfer as isotropic in the perpendicular plane we are referring to statistically averaged transfer. When sampling and averaging is limited, e.g. finite snapshots as in direct numerical simulation or directions as in observations are employed, then a residual dependence on the azimuthal directions might persist in the estimates. This dependence could be associated with the locally spatial and temporal fluctuations caused by large-scale structures in the perpendicular plane at large B_0, as observed by Zikanov & Thess (1998). Adequate coverage of azimuthal angles is required to obtain an accurate estimation of cascade rates. To further check the mutual impact of the time and angle averages, the effects of the sampling time will be discussed in the next subsection.

4.3. *Effects of time averaging*

In this subsection, the hyper-viscous cases will be used to demonstrate the effect of time averaging. At least two aspects of the time averaging are of central importance, one being the time interval (or sampling frequency) ΔT, and the other being the length of periods T. We can expect that, in our driven cases, the smaller ΔT and the longer T, the more reliable the statistics. The time interval ΔT ($\Delta T < T_e$, where T_e is the large-eddy turnover time) does not show significant impacts on the third-order structure function in our cases (figures are not shown here). Therefore, in the following analysis, we fix $\Delta T = 0.5T_e$ and

974 A20-14

focus on the effect of the length of periods T. These periods are within the statistically stationary periods listed in table 1.

Figure 5 shows the effect of the length of periods (or the number of time frames, F) on the third-order structure function. The third-order law at fixed θ and ϕ as (3.7), at fixed θ but ϕ averaged as (3.8) and both θ and ϕ averaged as (3.9) is shown in the left, middle and right columns, respectively. Three key observations can be made: (i) the direction-averaged profiles require fewer time frames (F) to converge than the profiles with fixed θ and ϕ. For instance, at $B_0 = 5$ the direction-averaged profiles converge with 36 time snapshots, while the profiles with fixed θ and ϕ are not converged until 72 time frames are employed; (ii) a smaller B_0 requires fewer time frames to converge. The required numbers of time frames for $B_0 = 0$ and $B_0 = 5$ to converge are approximately 10 and 70, respectively, without the directional average (figure 5a,d,g). These times are reduced to approximately 5 and 30, respectively, with directional averaging (see figure 5c,f,i); (iii) time averaging is not as effective as the angle coverage, indicated by the different peak values of non-direction-averaged and direction-averaged profiles in the anisotropic cases. Also, by comparing the three columns, the angle averaging makes the plateaus of these plots closer to the actual dissipation rate. For instance, at $B_0 = 5$, the converged profiles without angular averaging, with only azimuthal averaging and with both azimuthal and polar averaging attain peak values of 1.19, 1.09 and 0.98, respectively. This indicates that, compared with the time averaging, the angle averaging is a more effective way to make the calculation of the structure function converge.

5. Conclusions

Three-dimensional simulations of incompressible MHD turbulence with normal and hyper-viscosity were conducted with different externally supported (mean) uniform magnetic fields to systematically study the effect of external mean magnetic fields on the cross-scale energy transfer and the third-order law. Three different forms of third-order structure functions were calculated with or without averaging of the azimuthal and polar angles. The results show that, compared with the normal viscous cases, the hyper-viscosity elongates and separates the inertial range from the dissipation range, thus helping the examination of the above-mentioned forms of the third-order law.

The third-order laws governing the behaviour of third-order structure functions in the inertial range are among the few rigorous results about cross-scale energy transfer. Existing studies of energy transfer in the inertial range in MHD and space plasmas have had a particular leaning toward the use of the simplified third-order law under the assumption of isotropy, as implemented in (3.6) (also called the isotropic form). Although the isotropic form is notable in its simplicity and elegance, one should keep in mind that the isotropic assumption is required to arrive at this point. That is, the isotropic form assumes that the energy transfer across scales quantified along one direction is representative of the complex 3-D energy transfer. This inevitably conflicts with the anisotropic nature, especially for solar wind turbulence, which casts doubt on the widespread use of the isotropic form of the third-order law.

To resolve the limitation concerning the isotropic form of the third-order law, we investigate systematically the angular dependence of the energy transfer. As shown by our MHD simulations with varying mean magnetic fields, one can directly recognize that the radial component Y_ℓ of the energy flux Y varies systematically over the direction relative to the mean magnetic field (i.e. polar angle θ in spherical coordinates). If we only use the profile along one direction (i.e. choose a polar angle and an azimuthal angle)

to represent the energy transfer rate, it could depart significantly from the actual rate, necessitating simultaneous consideration of contributions from different directions to the energy transfer. The strategy developed by Taylor *et al.* (2003) is therefore employed, by which the third-order structure function is computed in many directions and the results are averaged, which is called the direction-averaging method (i.e. method III in (3.9)). We find that the direction-averaged third-order law can predict the energy cascade rates and inertial range accurately, even at very high B_0, thus providing a convincing scheme for extracting the energy transfer rate in anisotropic flows. The azimuthal angle dependence we find here is counterintuitive, in that the statistics are usually deemed to be statistically isotropic in the plane perpendicular to B_0. This azimuthal angle dependence was further confirmed with an examination of the number of averaging time frames. More time frames are required to make the calculation of the third-order structure function converge in the anisotropic condition, especially at high B_0. However, even using enough time frames, the structure function profiles with and without the azimuthal average are still different. We conclude that the time averaging cannot make up for a lack of angle averaging, especially at large values of the mean magnetic field B_0.

An interesting finding, also seen in earlier studies (Verdini *et al.* 2015; Wang *et al.* 2022), is that identified peaks or plateaus of the estimated transfer rate occur at different scales for different angles with respect to the mean magnetic field. Accordingly, this also means that the inertial range will be assigned to different ranges of scales at different angles. Our use of hyper-viscosity produces an extended plateau, facilitating analysis of the inertial range properties. Future studies may find a rationale for understanding how these different ranges come into being, as the balance of local transfer rate competes with dissipation at different angles. Such analyses may require examination of the vector character of the Yaglom energy flux, a subject that we have not engaged in here. It should be noted, however, that there are some studies that have begun such analyses, typically by making assumptions regarding the symmetry of the transfer. Examples include the 2-D (perpendicular) + 1-D (parallel) model employed by MacBride, Smith & Forman (2008), Stawarz *et al.* (2009) and Stawarz *et al.* (2010). Such models may require further refinement since at least some prior models enforce the questionable assumption that the transfers of energy in parallel and perpendicular directions are independent.

Declaration of interests. The authors report no conflict of interest.

Author ORCIDs.

Ⓓ Bin Jiang https://orcid.org/0000-0002-4858-0505;

Ⓓ William H. Matthaeus https://orcid.org/0000-0001-7224-6024;

Ⓓ Minping Wan https://orcid.org/0000-0001-5891-9579.

Appendix

To choose the hyper-viscosity coefficient (ν_h) and order (h), three different orders of hyper-viscosity (h) with 256^3 grids are tested, as shown in figure 6. We tuned the coefficient (ν_h) to ensure all these 3 test cases with $k_{max}\eta_{k,\nu} \sim 1.5$ to achieve a long
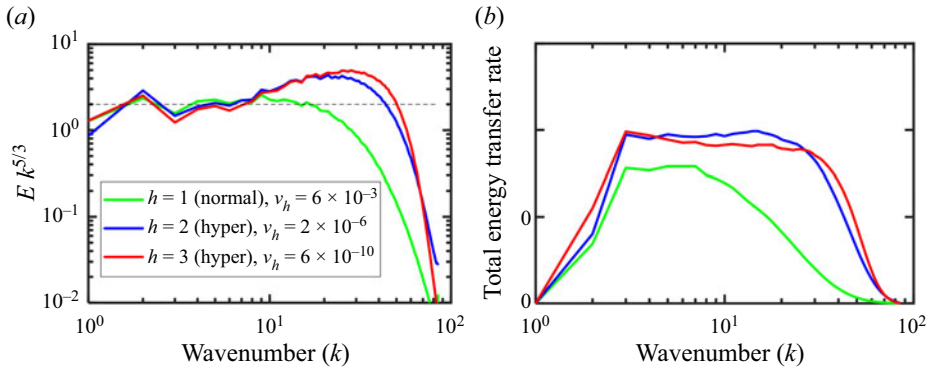
Figure 6. Comparison of the normal ($h = 1$) and hyper-viscous ($h = 2, 3$) cases at $B_0 = 0$ with 256^3 grids. (*a*) Compensated energy spectra; (*b*) energy transfer rate.
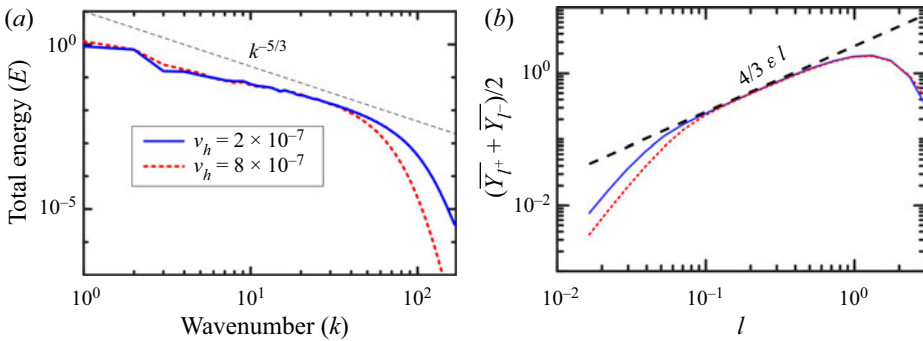

Figure 7. Comparison of the hyper-viscous ($h = 2$) cases with different viscosity coefficients at $B_0 = 0$ with 512^3 grids. (*a*) Energy spectra; (*b*) third-order structure function.

inertial range while resolving the dissipation range. It shows that the higher order ($h = 3$) of hyper-viscosity can further extend the inertial range, while the bottleneck effect is more obvious, as shown in the compensated energy spectra, consistent with Frisch *et al.* (2008). Following these tests we decided that the choice of $h = 2$ performs very well for our purposes.

To further evaluate the bottleneck effect, we also compared the choice of the hyper-viscosity coefficients with 512^3 grids at $h = 2$, as shown in figure 7. Both the energy spectra and structure function profiles show that the present hyper-viscosity with $\nu_h = 2 \times 10^{-7}$ and $k_{max}\eta_{k,\nu} = 1.73$ achieve the longer inertial range, compared with the larger ν_h at 8×10^{-7} with $k_{max}\eta_{k,\nu} = 2.47$. Furthermore, from the structure function profiles, this bottleneck effect is indeed not visible as per Biskamp & Müller (2000).

REFERENCES

ALEXAKIS, A. 2013 Large-scale magnetic fields in magnetohydrodynamic turbulence. *Phys. Rev. Lett.* **110**, 084502.

ALEXAKIS, A., BIGOT, B., POLITANO, H. & GALTIER, S. 2007 Anisotropic fluxes and nonlocal interactions in magnetohydrodynamic turbulence. *Phys. Rev.* E **76** (5), 056313.

ANDRÉS, N., SAHRAOUI, F., GALTIER, S., HADID, L.Z., FERRAND, R. & HUANG, S.Y. 2019 Energy cascade rate measured in a collisionless space plasma with MMS data and compressible Hall magnetohydrodynamic turbulence theory. *Phys. Rev. Lett.* **123**, 245101.

ANTONIA, R.A., OULD-ROUIS, M., ANSELMET, F. & ZHU, Y. 1997 Analogy between predictions of Kolmogorov and Yaglom. *J. Fluid Mech.* **332**, 395–409.

BANDYOPADHYAY, R., *et al.* 2020 In situ observation of Hall magnetohydrodynamic cascade in space plasma. *Phys. Rev. Lett.* **124**, 225101.

BANERJEE, S., HADID, L.Z., SAHRAOUI, F. & GALTIER, S. 2016 Scaling of compressible magnetohydrodynamic turbulence in the fast solar wind. *Astrophys. J. Lett.* **829** (2), L27.

BERESNYAK, A. & LAZARIAN, A. 2009 Comparison of spectral slopes of magnetohydrodynamic and hydrodynamic turbulence and measurements of alignment effects. *Astrophys. J.* **702** (2), 1190–1198.

BISKAMP, D. 2003 *Magnetohydrodynamic Turbulence*. Cambridge University Press.

BISKAMP, D. & MÜLLER, W.C. 2000 Scaling properties of three-dimensional isotropic magnetohydrodynamic turbulence. *Phys. Plasmas* **7** (12), 4889–4900.

BRIARD, A. & GOMEZ, T. 2018 The decay of isotropic magnetohydrodynamics turbulence and the effects of cross-helicity. *J. Plasma Phys.* **84** (1), 905840110.

BRUNO, R. & CARBONE, V. 2013 The solar wind as a turbulence laboratory. *Living Rev. Solar Phys.* **10** (1), 2.

CARBONE, V., MARINO, R., SORRISO-VALVO, L., NOULLEZ, A. & BRUNO, R. 2009 Scaling laws of turbulence and heating of fast solar wind: the role of density fluctuations. *Phys. Rev. Lett.* **103**, 061102.

COLEMAN, J.R. & PAUL, J. 1968 Turbulence, viscosity, and dissipation in the solar-wind plasma. *Astrophys. J.* **153**, 371–388.

DE KÁRMÁN, T. & HOWARTH, L. 1938 On the statistical theory of isotropic turbulence. *Proc. R. Soc. Lond.* A **164** (917), 192–215.

FERRAND, R., GALTIER, S., SAHRAOUI, F., MEYRAND, R., ANDRÉS, N. & BANERJEE, S. 2019 On exact laws in incompressible Hall magnetohydrodynamic turbulence. *Astrophys. J.* **881** (1), 50.

FERRAND, R., SAHRAOUI, F., GALTIER, S., ANDRÉS, N., MININNI, P. & DMITRUK, P. 2022 An in-depth numerical study of exact laws for compressible Hall magnetohydrodynamic turbulence. *Astrophys. J.* **927** (2), 205.

FRISCH, U. 1995 *Turbulence. The legacy of A. N. Kolmogorov*. Cambridge University Press.

FRISCH, U., KURIEN, S., PANDIT, R., PAULS, W., RAY, S.S., WIRTH, A. & ZHU, J.Z. 2008 Hyperviscosity, Galerkin truncation, and bottlenecks in turbulence. *Phys. Rev. Lett.* **101** (14), 144501.

GALTIER, S. 2009 Exact vectorial law for axisymmetric magnetohydrodynamics turbulence. *Astrophys. J.* **704** (2), 1371–1384.

GOGOBERIDZE, G., PERRI, S. & CARBONE, V. 2013 The Yaglom law in the expanding solar wind. *Astrophys. J.* **769** (2), 111.

HADID, L.Z., SAHRAOUI, F. & GALTIER, S. 2017 Energy cascade rate in compressible fast and slow solar wind turbulence. *Astrophys. J.* **838** (1), 9.

HELLINGER, P., TRÁVNIČEK, P.M., ŠTVERÁK, Š., MATTEINI, L. & VELLI, M. 2013 Proton thermal energetics in the solar wind: Helios reloaded. *J. Geophys. Res.* **118**, 1351–1365.

HELLINGER, P., VERDINI, A., LANDI, S., FRANCI, L. & MATTEINI, L. 2018 von Kármán–Howarth equation for Hall magnetohydrodynamics: hybrid simulations. *Astrophys. J. Lett.* **857** (2), L19.

HORBURY, T.S., FORMAN, M. & OUGHTON, S. 2008 Anisotropic scaling of magnetohydrodynamic turbulence. *Phys. Rev. Lett.* **101** (17), 175005.

HOSSAIN, M., GRAY, P.C., PONTIUS, D.H. JR., Matthaeus, W.H. & Oughton, S. 1995 Phenomenology for the decay of energy-containing eddies in homogeneous MHD turbulence. *Phys. Fluids* **7** (11), 2886–2904.

JOKIPII, J.R. & HOLLWEG, J.V. 1970 Interplanetary scintillations and the structure of solar-wind fluctuations. *Astrophys. J.* **160**, 745–753.

KOLMOGOROV, A.N. 1941*a* Dissipation of energy in the locally isotropic turbulence. *C.R. Acad. Sci. URSS* **32**, 16, [Reprinted in Proc. R. Soc. London, Ser. A **434**, 15–17 (1991)].

KOLMOGOROV, A.N. 1941*b* Local structure of turbulence in an incompressible viscous fluid at very high Reynolds numbers. *Dokl. Akad. Nauk SSSR* **30**, 301–305, [Reprinted in Proc. R. Soc. London, Ser. A **434**, 9–13 (1991)].

KRAICHNAN, R.H. 1971 Inertial-range transfer in two-and three-dimensional turbulence. *J. Fluid Mech.* **47** (3), 525–535.

KRITSUK, A.G., USTYUGOV, S.D., NORMAN, M.L. & PADOAN, P. 2009 Simulating supersonic turbulence in magnetized molecular clouds. In *Journal of Physics: Conference Series*, vol. 180, p. 012020. IOP Publishing.

MACBRIDE, B.T., SMITH, C.W. & FORMAN, M.A. 2008 The turbulent cascade at 1 AU: energy transfer and the third-order scaling for MHD. *Astrophys. J.* **679** (2), 1644–1660.

MATTHAEUS, W.H., *et al.* 2019 [plasma 2020 decadal] the essential role of multi-point measurements in turbulence investigations: the solar wind beyond single scale and beyond the Taylor hypothesis. arXiv:1903.06890.

MATTHAEUS, W.H., GHOSH, S., OUGHTON, S. & ROBERTS, D.A. 1996 Anisotropic three-dimensional MHD turbulence. *J. Geophys. Res.* **101** (A4), 7619–7629.

MATTHAEUS, W.H. & GOLDSTEIN, M.L. 1982 Measurement of the rugged invariants of magnetohydro-dynamic turbulence in the solar wind. *J. Geophys. Res.* **87** (A8), 6011–6028.

MILANO, L.J., MATTHAEUS, W.H., DMITRUK, P. & MONTGOMERY, D.C. 2001 Local anisotropy in incompressible magnetohydrodynamic turbulence. *Phys. Plasmas* **8** (6), 2673–2681.

MONIN, A.S., YAGLOM, A.M. 1975 *Statistical Fluid Mechanics*, Vol. 2. MIT Press.

NIE, Q. & TANVEER, S. 1999 A note on third-order structure functions in turbulence. *Proc. R. Soc. Lond.* A **455** (1985), 1615–1635.

OSMAN, K.T., WAN, M., MATTHAEUS, W.H., WEYGAND, J.M. & DASSO, S. 2011 Anisotropic third-moment estimates of the energy cascade in solar wind turbulence using multispacecraft data. *Phys. Rev. Lett.* **107**, 165001.

OUGHTON, S. & MATTHAEUS, W.H. 2020 Critical balance and the physics of magnetohydrodynamic turbulence. *Astrophys. J.* **897** (1), 37.

OUGHTON, S., MATTHAEUS, W.H., WAN, M. & OSMAN, K.T. 2015 Anisotropy in solar wind plasma turbulence. *Phil. Trans. R. Soc.* A **373** (2041), 20140152.

PARKER, E.N. 1979 *Cosmical Magnetic Fields: Their Origin and Activity*. Oxford University Press.

PODESTA, J.J. 2008 Laws for third-order moments in homogeneous anisotropic incompressible magnetohydrodynamic turbulence. *J. Fluid Mech.* **609**, 171–194.

PODESTA, J.J., FORMAN, M.A. & SMITH, C.W. 2007 Anisotropic form of third-order moments and relationship to the cascade rate in axisymmetric magnetohydrodynamic turbulence. *Phys. Plasmas* **14** (9), 092305.

POLITANO, H. & POUQUET, A. 1998 von Kármán–Howarth equation for magnetohydrodynamics and its consequences on third-order longitudinal structure and correlation functions. *Phys. Rev.* E **57** (1), R21.

SHEBALIN, J.V., MATTHAEUS, W.H. & MONTGOMERY, D. 1983 Anisotropy in MHD turbulence due to a mean magnetic field. *J. Plasma Phys.* **29** (3), 525–547.

SPENCE, H.E. 2019 HelioSwarm: unlocking the multiscale mysteries of weakly-collisional magnetized plasma turbulence and ion heating. In *AGU Fall Meeting Abstracts*, vol. 2019, pp. SH11B–04.

SPYKSMA, K., MAGCALAS, M. & CAMPBELL, N. 2012 Quantifying effects of hyperviscosity on isotropic turbulence. *Phys. Fluids* **24** (12), 125102.

STAWARZ, J.E., SMITH, C.W., VASQUEZ, B.J., FORMAN, M.A. & MACBRIDE, B.T. 2009 The turbulent cascade and proton heating in the solar wind at 1 AU. *Astrophys. J.* **697** (2), 1119–1127.

STAWARZ, J.E., SMITH, C.W., VASQUEZ, B.J., FORMAN, M.A. & MACBRIDE, B.T. 2010 The turbulent cascade for high cross-helicity states at 1 AU. *Astrophys. J.* **713** (2), 920–934.

STAWARZ, J.E., VASQUEZ, B.J., SMITH, C.W., FORMAN, M.A. & KLEWICKI, J. 2011 Third moments and the role of anisotropy from velocity shear in the solar wind. *Astrophys. J.* **736** (1), 44.

TAYLOR, G.I. 1938 The spectrum of turbulence. *Proc. R. Soc. Lond.* A **164** (919), 476–490.

TAYLOR, M.A., KURIEN, S. & EYINK, G.L. 2003 Recovering isotropic statistics in turbulence simulations: the Kolmogorov 4/5th law. *Phys. Rev.* E **68**, 026310.

TU, C. & MARSCH, E. 1995 MHD structures, waves and turbulence in the solar wind: observations and theories. *Space Sci. Rev.* **73** (1–2), 1–210.

VERDINI, A., GRAPPIN, R., HELLINGER, P., LANDI, S. & MÜLLER, W.C. 2015 Anisotropy of third-order structure functions in MHD turbulence. *Astrophys. J.* **804** (2), 119.

WAN, M., SERVIDIO, S., OUGHTON, S. & MATTHAEUS, W.H. 2009 The third-order law for increments in magnetohydrodynamic turbulence with constant shear. *Phys. Plasmas* **16** (9), 090703.

WAN, M., SERVIDIO, S., OUGHTON, S. & MATTHAEUS, W.H. 2010 The third-order law for magnetohydrodynamic turbulence with shear: numerical investigation. *Phys. Plasmas* **17** (5), 052307.

WANG, Y., CHHIBER, R., ADHIKARI, S., YANG, Y., BANDYOPADHYAY, R., SHAY, M.A., OUGHTON, S., MATTHAEUS, W.H. & CUESTA, M.E. 2022 Strategies for determining the cascade rate in MHD turbulence: isotropy, anisotropy, and spacecraft sampling. *Astrophys. J.* **937** (2), 76.

YANG, Y., LINKMANN, M., BIFERALE, L. & WAN, M. 2021 Effects of forcing mechanisms on the multiscale properties of magnetohydrodynamics. *Astrophys. J.* **909** (2), 175.

YANG, Y., MATTHAEUS, W.H., SHI, Y., WAN, M. & CHEN, S. 2017 Compressibility effect on coherent structures, energy transfer, and scaling in magnetohydrodynamic turbulence. *Phys. Fluids* **29** (3), 035105.

YOKOYAMA, N. & TAKAOKA, M. 2021 Energy-flux vector in anisotropic turbulence: application to rotating turbulence. *J. Fluid Mech.* **908**, A17.

YOSHIMATSU, K. 2012 Examination of the four-fifths law for longitudinal third-order moments in incompressible magnetohydrodynamic turbulence in a periodic box. *Phys. Rev.* E **85** (6), 066313.

ZHAI, X.M. & YEUNG, P.K. 2018 Evolution of anisotropy in direct numerical simulations of MHD turbulence in a strong magnetic field on elongated periodic domains. *Phys. Rev. Fluids* **3** (8), 084602.

ZIKANOV, O. & THESS, A. 1998 Direct numerical simulation of forced MHD turbulence at low magnetic Reynolds number. *J. Fluid Mech.* **358**, 299–333.